Design Considerations for High-Current Photodetectors

Keith J. Williams, *Member, IEEE,* and Ronald D. Esman, *Senior Member, IEEE, Member, OSA*

Abstract— **This paper outlines the design considerations for gigahertz-bandwidth, high-current p-i-n photodiodes utilizing InGaAs absorbers. The factors being investigated are photodetector intrinsic region length, intrinsic region doping density, temperature effects, illumination spot size, illumination wavelength, frequency, and illumination direction. Space-charge calculations are used to determine optimal device geometry and conditions which maximize saturation photocurrent. A thermal model is developed to study the effects of temperature on high-current photodetector performance. The thermal and space-charge model results are combined to emphasize the importance of thin intrinsic region lengths to obtain high current. Finally, a comparison between surface-illuminated p-i-n structures and waveguide structures is made to differentiate between the problems associated with achieving high current in each structure and to outline techniques to achieve maximum performance.**

Index Terms—**Heating, nonlinearities, photodetectors, photodiodes, p-i-n photodiodes, semiconductor device modeling, thermal factors.**

I. Introduction

MANY microwave and millimeter-wave photonic systems benefit with the use of high-current photodetectors. The use of high photocurrent increases the dynamic range and reduces the loss and noise figure in externally modulated links [1]–[3] and can decrease the complexity of high-bit-rate digital receivers [4], [5]. Increasing the output photocurrent also increases the output radio frequency (RF) signal level possible directly from the photodetector. This point is particularly important in optically steered phased array antennas since any increase in photodetector output signal level reduces the necessary phase- and amplitude-matched electronic gain at each antenna element. In an effort to increase the output photocurrent, a number of groups have been studying surface-illuminated [6]–[11], metal-semiconductor-metal [12], [13], waveguide [14], [15], traveling-wave [16], [17], and photodetector arrays [18], [19]. The ability to increase photocurrent depends on two primary factors: 1) space-charge limitations which are influenced by physical dimensions, structure type, illumination conditions, maximum electric field, etc. and 2) thermal considerations. Whether space-charge or thermal effects ultimately limit the maximum photocurrent has yet to be determined, however, thermal effects are important, especially for the long-term reliability of photodetectors. This paper addresses some of the design issues and tradeoff's for high-current photodetectors.

Manuscript received February 9, 1999; revised May 6, 1999. This work was supported in part by the Office of Naval Research.

The authors are with the Naval Research Laboratory, Washington, DC 20375 USA (e-mail: keith.williams@nrl.navy.mil).

Publisher Item Identifier S 0733-8724(99)06333-1.

II. General Considerations

The realization of high-current photodetectors (PD's) can be greatly enhanced through careful design and packaging. To maximize photocurrent, some design tradeoff's are necessary, some of which are not compatible with designs that maximize quantum efficiency or that have wide packaging tolerances. However, the performance lost can be minimal while providing for substantial improvements in photocurrent. Quite often these tradeoff's are interrelated, so the consequences need to be evaluated from all aspects to obtain whether a particular design trade is warranted. For example, space-charge effects can be reduced simply by increasing the applied PD voltage, however, larger PD bias voltages increases the risk of electrical breakdown due to a high-peak electric field and shortened lifetime due to increased Joule heating. The obvious trades are those which have little or no consequences such as the choice to illuminate through the p-side rather than the n-side of the device. Such choices can result in an order of magnitude improvement in saturation current [11], depending on the frequency, intrinsic region thickness, and illumination wavelength.

The design of high-current PD's relies on measurement and simulation techniques which can provide insight into the cause and effect of such design trades. A two-laser heterodyne system [20] has been used to characterize PD nonlinearities [3], [20], [21] as well as the large-signal saturation behavior [22], and pulsed systems [17], [18], [23] are helpful in studying the transient behavior. Small-signal measurement systems have also been used to measure certain characteristics [6], [7], [11], [14], [22]–[24] of high-current PD's. A particular implementation of a small-signal measurement system is shown in Fig. 1, where the outputs of a constant-power RF-modulated laser are combined with a variable high-power continuous wave (CW) laser and illuminate the PD under test. The lasers operate at slightly separated wavelengths to prohibit the generation of detectable beat frequencies, but close enough to ensure good overlap of the incident optical fields—difference wavelengths from 1 to 10 nm is a good compromise. Larger wavelength differences can yield erroneous results since the probe and dc fields may not sufficiently overlap or there may be significant wavelength dependence [11] in the response. More than 60 dB of total isolation (30 dB internal and 30 dB external to each laser) is maintained between lasers to prohibit reflections from influencing the RF-modulated optical power illuminating the

U.S. Government work not protected by U.S. copyright.

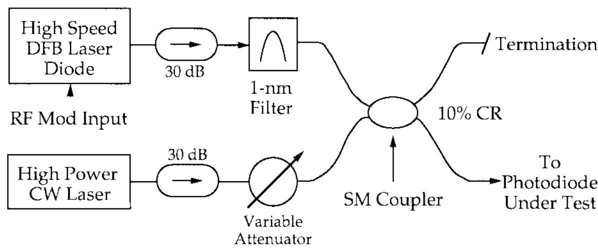

Fig. 1. Small-signal compression response measurement system.

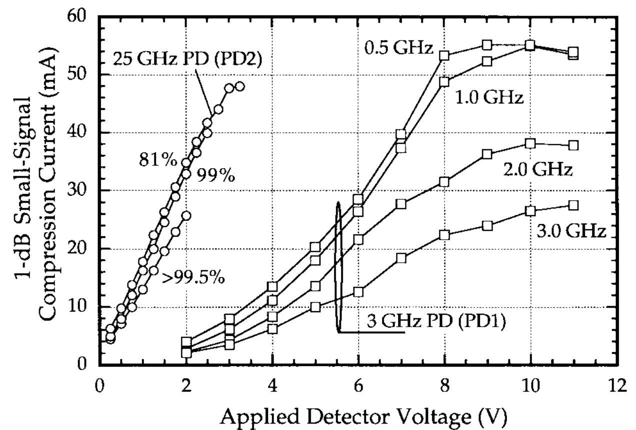

Fig. 2. Measured small-signal 1 dB compression currents at 1319 nm for a 75 μm diameter 3 GHz photodetector (PD1, squares) at test frequencies of 0.5, 1, 2, and 3 GHz and for a 25 μm diameter 25 GHz photodetector (PD2, circles) at a test frequency of 10 GHz. For the 25 GHz photodetector, the incident light was expanded to overfill the active area until the quantum efficiency decreased from its maximum value to 99.5, 99, and 81%.

PD. Thus, the incident RF-modulated light is independent of the average CW laser power.

The system in Fig. 1 is used to measure the small-signal 1 dB compression current, $I_{1\text{-dB},\,ss}$, as a function of applied PD bias. The RF response at a particular fixed frequency of the PD under test is monitored as the average current is increased. The RF photoresponse decreases at high average illumination levels due to a buildup of carriers in the depletion region, accompanied by a partial collapse of the intrinsic region electric field [6]. The current at which the response decreases by 1 dB from the value at low currents is denoted $I_{1\text{-dB},\,ss}$. This definition of compression is used here and is appropriate for quadrature-biased externally modulated links or other systems where predominantly high average currents are encountered. Alternative definitions of compression for pulsed [18] or large-signal [22] CW conditions are more appropriate for those particular applications and will not be considered here. Direct comparisons between $I_{1\text{-dB},\,ss}$ measurements and measurements based on these alternative definitions should be avoided as pulsed compression measurements tend to result in much higher compression currents and are dependent on pulse width [23] while large-signal compression measurements typically lead to lower compression currents [22] due to the higher peak currents. In general, $I_{1\text{-dB},\,ss}$ is a function of RF frequency, with higher frequencies exhibiting larger compression for the same average current. The measurement can also be influenced by quantum efficiency nonlinearities [24] which can increase or decrease the response as well as being a function of frequency.

Small-signal compression measurements are shown in Fig. 2 for two devices: a 3 GHz p-side-illuminated p-i-n [11], denoted PD1, and a 25 GHz n-side-illuminated p-i-n, denoted PD2, and similar to those in [25] except with a 0.5-μm long intrinsic region. Note that the 3 GHz PD shows behavior typical of space-charge limited currents, with higher frequencies displaying lower $I_{1\text{-dB},\,ss}$. The differences in the response of PD2 will be discussed in Section III. Several typical characteristics are readily obtained from the measurements in Fig. 2. First, there is a threshold voltage, V_{th}, where the slope of $I_{1\text{-dB},\,ss}$ increases sharply. As will be shown shortly, minimizing V_{th} is important, since large V_{th} force large PD bias voltages which contribute to Joule heating in the absorber, where elevated temperatures can lead to catastrophic failure [8]. For PD1 and PD2, V_{th} is approximately 4 and 0 V, respectively. Second, the slope, α, of $I_{1\text{-dB},\,ss}$ versus voltage is important since this also necessitates added bias for maintaining linearity at a given current. In Fig. 2, α is in the range of between 5–16 mA/V. This paper will discuss ideas for minimizing V_{th} and maximizing α.

To analyze Joule heating in the absorber, an expression relating the dissipated power to the necessary applied voltage and photocurrent can be derived with the help of a model [Fig. 3(a) and (b)] for a typical biased PD. A dc voltage bias (V_{bias}) is applied across the junction with a bias tee. In addition to the V_{bias} requirements imposed to maintain PD linearity (determined by α and V_{th}), load voltage transients also necessitate higher V_{bias}. Fig. 3(b) shows the dynamic voltage and current characteristics of the PD and load impedance configuration of Fig. 3(a). As the RF current flows through the load, the induced load voltage causes the PD terminal voltage to vary around its dc level. Thus, under large-signal operation, to keep the PD terminal voltage greater than 0 V (reversed biased), V_{bias} must be greater than $I_{\text{peak}} * R_{\text{load}}$. Increasing V_{bias} to account for load voltage transients will increase the PD junction power dissipation for all modulation depths, emphasizing the need to minimize the PD voltage required to overcome space-charge effects. V_{bias} is thus the sum of three terms, the peak load voltage, $V_{pk\text{-load}}$, a term proportional to the inverse-slope of $I_{1\text{-dB},\,ss}$, α, and the minimum voltage required for high current operation, V_{th}.

Conservation of energy dictates that the power dissipated P_{det} in the PD depletion region can be expressed as

$$P_{\text{det}} + P_{\text{load}} = P_{\text{bias}} + P_{abs} \tag{1}$$

where P_{bias} is the power supplied by the voltage source and P_{load} is the power delivered to the load. P_{abs} is the absorbed optical power that results in dc photocurrent, equal to the incident power multiplied by the PD quantum efficiency. Incident light that does not contribute to the dc photocurrent does not contribute significantly to heating, so, it is neglected in this analysis. The power supplied by the bias source is just the average current multiplied by V_{bias}. Therefore, the

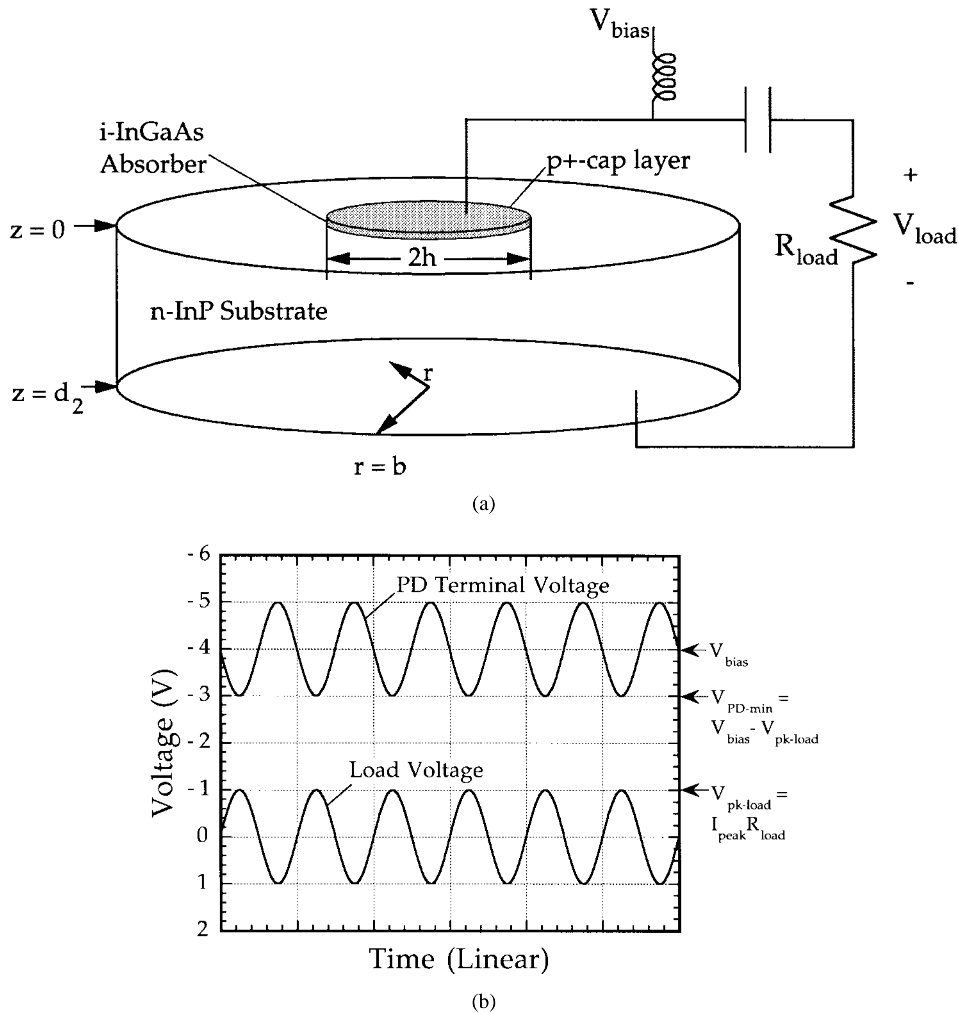

Fig. 3. (a) Mesa photodetector bias circuit and physical geometrical and (b) transient PD terminal and load voltages and currents. The frequency of the sine wave in (b) is assumed to be high enough such that the impedance of the capacitor in (a) is negligible.

minimum bias source power is given by

$$P_{\text{bias, min}} = I_{ave}\left(V_{pk\text{-load}} + \frac{2I_{ave}}{\alpha} = V_{th}\right). \quad (2)$$

The first term represents the minimum dc PD terminal voltage required to maintain a terminal voltage greater than 0 V while delivering V_{pk} to the load. The second and third terms represent the necessary bias for the PD to operate at high currents. The factor of two in the second term accounts for the possibility of large-signal (100% modulation depth) operation. For ac-coupled 100% modulation depths (Fig. 3), the average current is just the peak load voltage divided by the load resistance, R, thus substituting (2) into (1) yields

$$P_{\text{det}} = \left(\frac{V_{pk\text{-load}}}{R}\right)\left(1 + \frac{2}{\alpha R} + \frac{V_{th}}{V_{pk}}\right) + P_{abs} - P_{\text{load}}. \quad (3)$$

The photodetector power conversion efficiency η is defined as

$$\eta = \frac{P_{\text{load}}}{P_{\text{det}}}. \quad (4)$$

The first term in (3) equals $2P_{\text{load}}$, which reduces (4) to

$$\eta = \frac{1}{\left(1 + \frac{4}{\alpha R} + \frac{2V_{th}}{V_{pk\text{-load}}} + \frac{P_{abs}}{P_{\text{load}}}\right)}. \quad (5)$$

For an ideal (although unrealizable) high current PD, α is infinite and $V_{th} = 0$, implying from (5) that η can approach 100% ($P_{abs} \ll P_{\text{load}}$ and assuming 100% QE).

When the PD has finite α and nonzero V_{th}, the decrease in η can be quite substantial. Fig. 4 plots (3) for three different PD's, labeled (a), (b), and (c). The ideal high current PD (curve a) represents infinite α and $V_{th} = 0.0$, thereby representing the minimum power that the PD absorber must dissipate to deliver a given output power. Curve (b) represents a PD similar to PD2 which does not require any excess bias voltage for high current operation ($V_{th} = 0.0$) but requires additional voltage to overcome space-charge effects (finite α). This is nearly the case for PD2 (Fig. 2) where $V_{th} \sim 0$ V and $\alpha = 16$ mA/V. Note that at +20 dBm output (100 mW RF power), the power conversion efficiency decreases from 61% for curve (a) to 15% for curve (b), more than four times the power dissipation

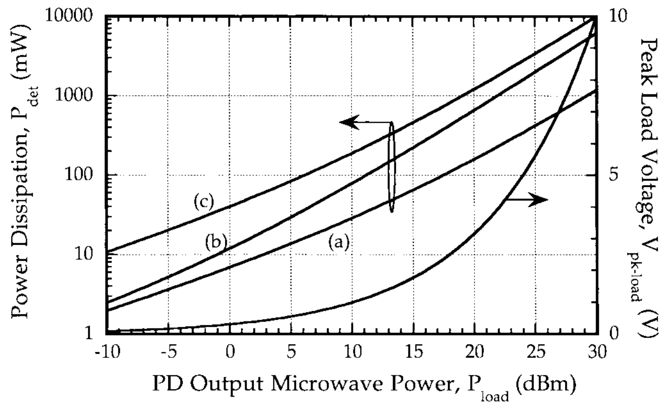

Fig. 4. Calculated depletion region power dissipation versus output microwave power per equation (3) for: (a) an ideal high current photodetector with α infinite and $V_{th} = 0$, (b) $\alpha = 16$ mA/V, and $V_{th} = 0$, and (c) $\alpha = 10$ mA/V and $V_{th} = 4$ V. The peak load voltage is also plotted for reference.

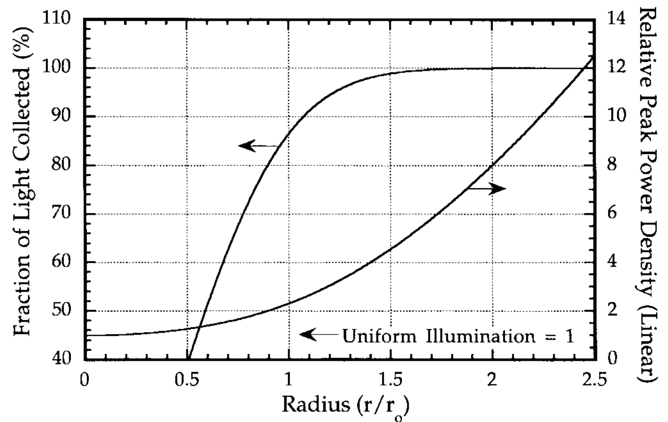

Fig. 5. The fraction of light collected by a circular absorber of radius, r, with an incident beam radius, r_o (e^{-2} intensity). Also plotted is the relative peak power density which is defined as the peak power density (beam center) divided by the power density of a uniform illuminated PD at the same average current.

in the absorber. Curve (c) represents a PD similar to PD1 (Fig. 2) where in addition to having finite α, the PD requires a minimum voltage, V_{th}, before the current handling capacity of the PD increases. This further reduces η, where at +20 dBm output, η decreases to 8%. Fig. 4 clearly emphasizes the need to maximize α and minimize V_{th} in high-current PD's, especially as output powers increase to above +10 dBm, and as power dissipations increase above 100 mW. In Section V, the PD thermal impedance will be analyzed to show that such high power dissipation levels can result in catastrophic failure.

III. Optical Power Density Considerations

In the previous section it was shown how important it is to maximize the slope, α. The slope is determined primarily by space-charge effects where the separation of photogenerated carriers yields an opposing space-charge electric field which redistributes the intrinsic region electric field, causing the field to collapse [6], resulting in RF compression. Thus, higher intrinsic-region electric fields (applied voltages) are required to increase compression current. The first step to minimizing the space-charge effects, hence increasing α, is to uniformly illuminate the absorber to minimize the photogenerated carrier densities. With a Gaussian beam incident on a circular absorber, the tradeoff that is made when designing for high power is to expand the beam diameter, however, this causes a fraction of the incident beam to "miss" the active region, resulting in lower quantum efficiencies. For this reason, most commercial PD's are not optimized for high power.

It has been shown [7] that by expanding the Gaussian beam such that 5–10% of the light misses a circular absorbing region, the compression current can double for the same applied voltage. The measurements for PD2 in Fig. 2 show that for less than a 1% quantum efficiency reduction, a 30% increase in compression current can be obtained. Using straightforward Gaussian beam calculations, the fraction of light captured and the relative peak power density are plotted in Fig. 5 as a function of the aperture radius (PD physical radius) divided by the beam e^{-2} intensity radius. The relative peak power density is the peak power density at the center of the expanded Gaussian beam normalized to a PD illuminated with uniform power density at the same total current. It can be seen that a ~10% reduction in collection efficiency (from 99.3 to 90%) reduces the relative peak power density by 50% (from 5.0 to 2.5). Thus, since compression is dominated by the highest power density regions in the PD, one should expect a corresponding increase in compression current. This increase has been experimentally confirmed for a 500 μm diameter PD [7], but for PD2 (25 μm diameter, Fig. 2), a reduced increase was observed for beam diameters resulting in less than 99% collection efficiencies. Nevertheless, the compression current did improve by up to 33% with the more uniform intensity distribution.

The results in Fig. 5 also suggest that substantially lower power densities can be obtained without compromise by slightly expanding the beam diameter. The peak power density can be reduced 50% by increasing the beam diameter from 1/2.5 to 1/1.7 times the physical diameter. This comes at the expense of only a 0.3% quantum efficiency reduction. Illumination with more complex optical systems which yield uniform intensity profiles could further lower the power density in surface-illuminated PD's. This would minimize photogenerated carrier densities, thus increasing performance (increased α), without sacrificing significant efficiency.

IV. Illumination Direction and Wavelength

In addition to minimizing the illuminated power density, the compression current for a RC-limited-bandwidth PD (area/thickness = constant) can be maximized with proper design of the semiconductor internal structure. One optimization technique has been modeled and verified [11] for 3 GHz PD's. The optimization is the result of differences between n- and p-side illumination for PD's with low-doped n-type absorbers. The results [11] suggest that illumination from the p-side with an absorber thickness equal to approximately two absorption lengths yields from two to ten times the compression current of identical PD's (same illumination

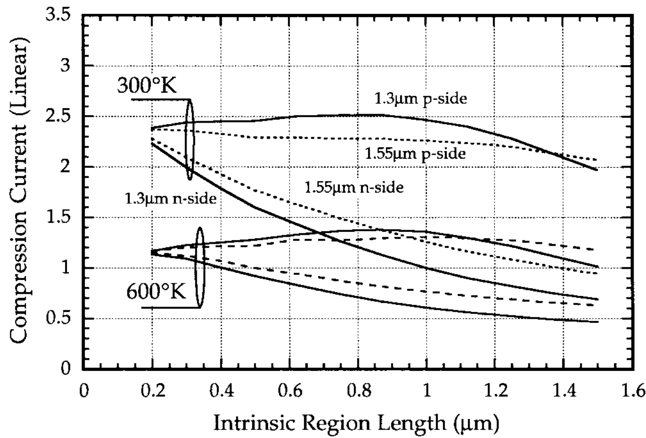

Fig. 6. Simulated compression current at a fundamental frequency of 10 GHz versus device intrinsic region length, illumination wavelength, and direction. The data is normalized to an n-side illuminated 1-μm long photodetector at 1319 nm and 300 K, at an average electric field strength of 100 kV/cm.

area, electric-field strength, and material structure) illuminated from the n-side. Fig. 6 shows simulation results for 20 GHz PD's. To compute the compression current, the diode harmonic distortion is calculated from the simulated sinusoidal response. As in [11], the current for which the second-harmonic distortion increases above -40 dBc is defined, for convenience, as the compression point. While this does not give an exact calculation for the compression current, it can be used as a consistent point near compression for comparisons between different PD structures. To make a fair comparison between PD's with different absorber lengths, a PD with a RC-limited bandwidth is assumed. Therefore, the illumination area is adjusted as the intrinsic region length is changed to keep their ratio constant. And, since the compression current scales with electric field, the applied voltage is adjusted as the intrinsic region length changes to yield the same average electric field strength throughout the absorbing region. The compression current is normalized to (divided by) an n-side illuminated 1-μm long PD at 1319 nm. The four curves at each temperature (in Fig. 6) are for p-side and n-side illumination at both 1.3 and 1.55 μm. The simulations are performed at both 300 and 600K to reflect the influence of temperature on the carrier mobilities and velocities. For 20 GHz p-side illuminated PD's, the optimum absorption thickness appears to be near one absorption length, although at 300 K, the maximum is quite broad, showing only a 5% difference between PD's with 0.25–1.1 μm absorber lengths. For InGaAs PD's with higher bandwidths, the advantages of illumination from the p-side dwindle, since the absorber thickness decreases due to transit time limitations and results in an absorption profile (absorbed power over the intrinsic region length) that is independent of position.

Since the differences in compression current between n- and p-side illuminated PD's is related to the steady-state distribution of carriers [11], small changes in the carrier velocities will have an effect on the calculated results (Fig. 6). More specifically, as the absorber temperature increases, any change in the ratio of hole to electron velocity can cause the position where the hole density equals the electron density to move, thus modifying the shape of the curves in Fig. 6. In addition, any proportional decrease in both hole and electron velocities will proportionally decrease the compression current at high electric fields since the carrier densities in the intrinsic region are roughly inversely proportional to velocity. For InGaAs, the carrier mobilities and saturated velocities can be approximated with T^{-m} temperature dependencies for T above 200K. The value of m is estimated from data in the literature to be $m = 0.7$ [26] and $m = 0.5$ [27], [28] for the electron mobility and high-field saturated velocity, respectively. For holes, $m = 0.85$ [26] for the mobility and $m = 0.7$ is used for the high-field saturated velocity. The temperature dependence of the saturated hole velocity was estimated from data for GaAs [29] due to the lack of information available for InGaAs. Since $0.5 < m < 0.85$ in all cases, the hole and electron velocities decrease by approximately the same fraction as T increases from 300 to 600 K. Therefore, the high temperature compression current data calculated in Fig. 6 shows primarily a decrease in overall compression current, due to the reduced velocities. This is in contrast to GaAs where $m = 1$ and 2.1 [30] for the electron and hole mobilities, respectively. Therefore, at moderate electric-field strengths, the optimum absorber length and the compression current are stronger functions of temperature for GaAs PD's.

V. Intrinsic Region Doping

High levels of unintentional intrinsic region doping can lead to high V_{th} and low α, and thus to excessive heating. Heat, as will be shown in the next section, can be the limiting factor in obtaining high-compression currents. Even moderate n-type intrinsic region doping densities can cause large excess heat generation by requiring more applied bias to fully deplete the intrinsic region. Fortunately, careful intrinsic region design can minimize V_{th}, thus minimizing the excess heat generated. Using Poisson's equation, the electric field, E, in a semiconductor void of free carriers (intrinsic region under dark conditions) is given by

$$E = \frac{q}{\varepsilon} \int (N_d - N_a) \tag{6}$$

where N_d and N_a are the donor and acceptor concentrations, respectively. For high-quality intrinsic material [26], $N_d - N_a$ is typically between 0.2 and 1.0×10^{15} cm^{-3} and predominately n-type. Thus, for a uniform distribution of donors in the intrinsic region, the electric field linearly decreases from the p-region to the n-region. As an example, the electric field strength under dark conditions ($E_{\rm dark}$) is plotted in Fig. 7 for a p-i-n PD with a 1-μm long intrinsic region under 10 V bias at several doping densities. Note how E decreases linearly throughout the intrinsic region. It has been previously shown [6], [11] that, as the PD nears compression, the electric field near the n-region ($X = 1.4$ μm in Fig. 7) approaches zero. This is due to a space-charge electric field (E_{sc}) component, which is proportional to the photocurrent, that opposes $E_{\rm dark}$. When the magnitude of E_{sc} equals $E_{\rm dark}$,

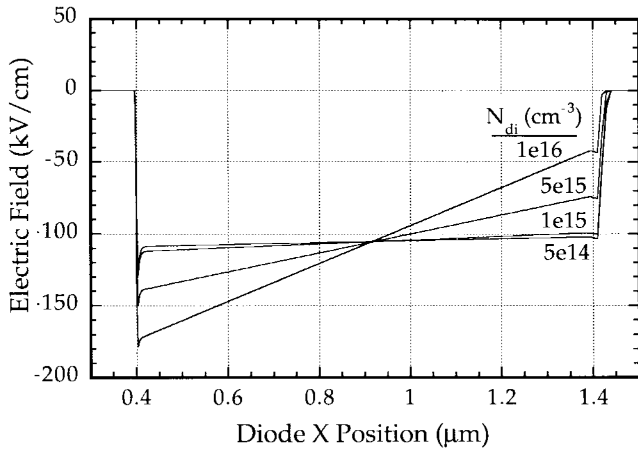

Fig. 7. Electric field for a 1-μm long intrinsic region photodetector under dark conditions for various n-type intrinsic region (uniform) doping densities. The intrinsic region extends from $X = 0.4$ to 1.4 μm.

the total E approaches zero. Thus, if E_{dark} is reduced near the n-region due to an increased intrinsic region doping level, a smaller E_{sc} (and thus a lower current) is needed to yield zero E.

To help quantify the effect that intrinsic region doping has on V_{th}, our numerical model will be used to evaluate several intrinsic region lengths and doping densities. Fig. 8(a)–(c) represents the compression current calculations for three PD's with intrinsic region lengths of 0.5, 1.0, and 1.25 μm, respectively, and with varying levels of n-type intrinsic region doping densities (N_{di}). Fig. 8(a)–(c) contains calculations for both n-side (solid lines) and p-side (dashed lines) illumination conditions. All compression current calculations are normalized to an n-side illuminated 1-μm long PD at 10 GHz. V_{th} can be seen from the figures to be approximately 0.4, 1.5, and 2.0 V for p-side illumination ($N_{di} < 1 \times 10^{15}$ cm^{-3}), and approximately 0.8, 3.0, and 4.5 V for n-side illumination ($N_{di} < 1 \times 10^{15}$ cm^{-3}) with 0.5, 1.0, and 1.25-μm long intrinsic regions, respectively.

Several important features of V_{th} are readily observed from Fig. 8(a)–(c). First, for p-side illumination, V_{th} is less sensitive to doping density for N_{di} below 5×10^{15} cm^{-3}. However, for n-side illumination, N_{di} must be less than 1×10^{15} cm^{-3} before the PD is insensitive to doping level. Second, V_{th} for p-side illumination is about half of V_{th} for the same PD illuminated from the n-side. Third, V_{th} increases with the intrinsic region length, and fourth, V_{th} for n-side illuminated PD's decreases substantially as the doping level increases. These results confirms one's intuition that low intrinsic region doping is beneficial to high current operation. Not only does V_{th} decrease with thinner intrinsic region lengths, but α also increases since the average intrinsic region electric field is equal to the applied voltage divided by intrinsic region length. Thus, thinner absorber region lengths will be increasingly important in minimizing the absorber power dissipation.

The compression current also has significant frequency dependence [6], [21]. As reported in [11] at 1 GHz, the optimum absorber thickness was near 2 μm for p-side illuminated PD's

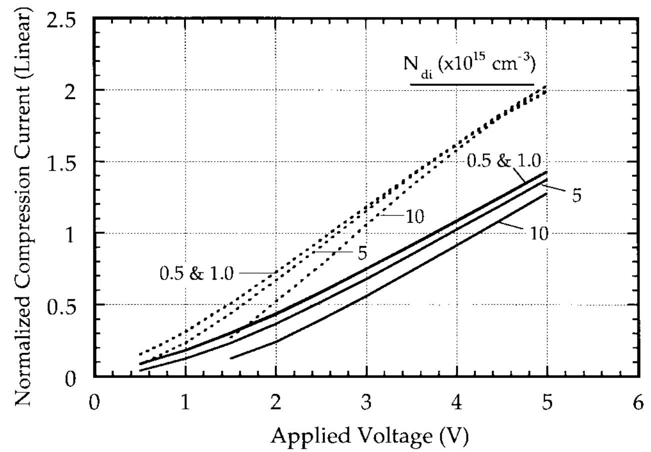

(a)

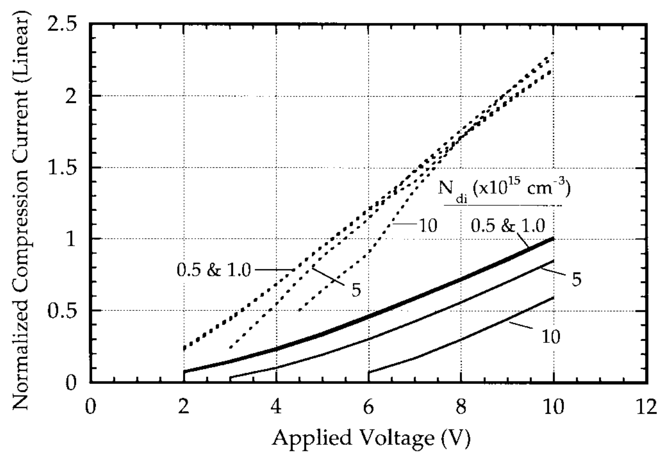

(b)

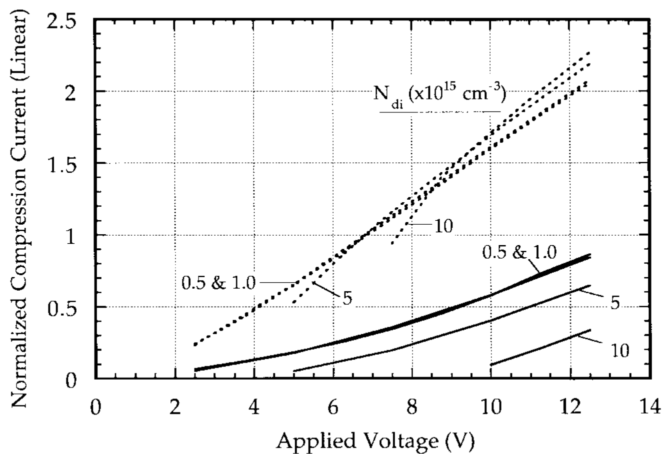

(c)

Fig. 8. Calculated compression current versus applied voltage for p-side (dashed) and n-side (solid) illuminated PD's with intrinsic region lengths of: (a) 0.5 μm, (b) 1.0 μm, and (c) 1.25 μm at various n-type intrinsic region uniform doping densities. The data is normalized to a n-side illuminated 1-μm long photodetector at 1319 nm and 300 K.

at 1.3 μm. This is in contrast to an optimum thickness of 0.8 μm for p-side illumination at 10 GHz (Fig. 6). To highlight these frequency differences, simulation results for a 0.5 and 1.0-μm long intrinsic region PD are plotted in Fig. 9(a) and (b), respectively, for various stimulus frequencies. As before,

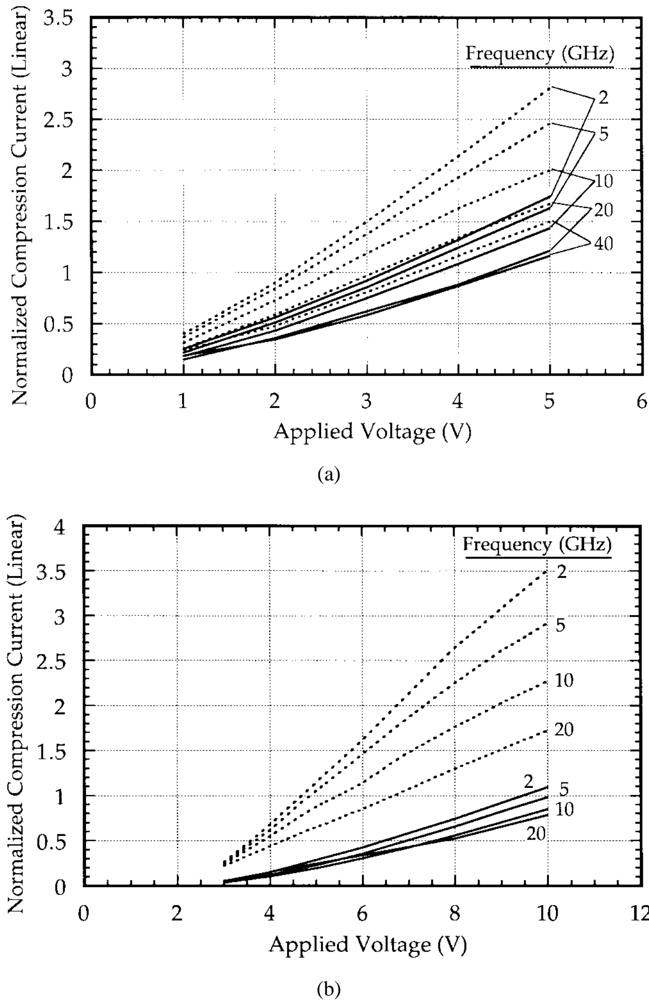

Fig. 9. Calculated compression current versus applied voltage for p-side (dashed) and n-side (solid) illuminated PD's with intrinsic region lengths of: (a) 0.5 μm and (b) 1.0 μm at various frequencies. The data is normalized to a n-side illuminated 1-μm long photodetector at 1319 nm and 300 K. The intrinsic region doping density is (a) 1×10^{15} cm^{-3} and (b) 5×10^{15} cm^{-3}.

the simulated compression current results are normalized to a 1.0-μm long n-side illuminated PD at 10 GHz. Note in both figures that V_{th} is roughly independent of frequency for both n- and p-side illumination conditions and an increase in slope accounts for the variation in compression current with frequency. Now, having a quantitative understanding of the space-charge limitations to obtaining high current, the thermal limitations will be quantified and incorporated into the design process to provide an overall optimization scheme for achieving high current.

VI. Thermal Considerations

Photodiode failure has been observed [31] to occur along curves of constant electrical power dissipation (bias voltage times photocurrent). This suggests a failure mechanism with thermal origins. Paslaski *et al.* [8] have studied the thermal behavior of PD's and have found that dark current runaway can explain failure. A thermally activated dark current causes PD failure when the dark current increase (due to a temperature rise) causes an additional increase in the diode temperature, resulting in additional dark current, and so on (thermal runaway). An interesting result from this analysis [8] is that the peak temperature within the InGaAs absorber reaches 900–1100 K at failure, depending on bias voltage, and the failure threshold is sharp. Given that PD failure can be linked to an increase in absorber temperature, a thermal model will be developed here to understand the limitations temperature has on the maximum compression current, thus allowing thermal optimization for a given structure. In this work, a detailed thermal model will be formed for surface-illuminated and waveguide-style PD's, with some discussion devoted to achieving optimum conditions.

The surface-illuminated PD to be modeled is shown in Fig. 3 where a circular mesa structure is shown. The heat is assumed to be generated evenly throughout the InGaAs absorber and flows only into the substrate. Since the optical beam may not uniformly fill the device area, the heat is concentrated slightly in the center of the absorber. In addition, there is a small nonuniformity of heat generated in the absorber due to the variations in electric field strength (hence, voltage drop variations), when high currents or slightly n-type absorbers ($>10^{15}$ cm^{-3}) are considered. The flow of heat, governed by Fourier's equation [32], reduces to Laplace's equation for steady-state CW conditions. For the special case of one-dimensional (1-D) heat flow between surfaces of constant temperature with a uniform heat source on one surface, the solution for the temperature between the two surfaces can be described with the use of the thermal impedance θ as

$$\theta = \frac{\Delta T}{P} = \frac{\Delta x}{kA} \tag{7}$$

where ΔT is the temperature difference between surfaces, P is the uniform heat source on one surface, Δx is the distance between surfaces, A is the surface area, and k is the thermal conductivity of the material. Equation (7) can be very useful in describing the thermal impedance of the absorber region of the PD in Fig. 3, as the absorber is usually very thin relative to its diameter, resulting in very little lateral heat flow. The heat flow from the bottom surface of the absorber through the mesa and substrate is two-dimensional (2-D). Accounting for the thermal impedance due to this region will be discussed shortly. However, it is important to first discuss the temperature rise of the absorber itself, as it is common to most PD structures, including waveguide, both lumped and traveling-wave designs, and surface illuminated p-i-n PD's. It is simple to show that the thermal impedance of a region with a uniform distribution of heat generation is equivalent to having all the heat generated at a plane in the absorber center. Thus, the thermal impedance for an InGaAs absorber with thickness d_1 and radius r is given by (7) and is equal to

$$\theta_{abs} = \frac{d_1/2}{k_1 \pi r^2} \tag{8}$$

where k_1 is the thermal conductivity of InGaAs. The temperature rise can then be calculated by multiplying (8) by the power dissipated in the absorber.

The thermal conductivity of many semiconductors decreases [33] with increasing temperature. For the materials of interest to long-wavelength PD's (InP, InGaAs, and InGaAsP) the temperature dependence of k can be approximated [34] as

$$k(T) = \frac{k(T_o)T_o^c}{T^c} \tag{9}$$

where T is the temperature, c is a constant in the range of $1.2 \leq c \leq 1.55$, and T_o is a temperature where k is equal to $k(T_o)$. Equation (9) is good approximation [34] for k in the range of T_o from 150 to 600 K, with $c = 1.375$ and 1.55 for InGaAs and InP, respectively. Since k is a function of temperature, a direct solution to Laplace's equation is a function of temperature and requires nonlinear calculations. Since the only temperature dependence is with k, Joyce [35] has shown that a Kirchoff transformation can be used to immediately yield the nonlinear solution from the linear solution which assumes constant k. Using the equations derived in [35], the relationship between the temperature rise, T, and the power dissipated, P, is

$$\theta_o P = \frac{1}{k(T_o)} \int_{T_o}^{T} k(T)\, dT \tag{10}$$

where θ_o is the thermal impedance from the solution to Laplace's equation with constant k. Substituting (9) into (10) and solving for T yields (valid for $c \neq 1$)

$$T = \exp\left\{ \frac{\ln\left(\frac{T_o + (1-c)\theta_o P}{T_o^c} \right)}{1-c} \right\}. \tag{11}$$

Using (8) and (11), the maximum absorber temperature rise for several uniformly illuminated circular InGaAs absorbers (k_1(300 K) $= 0.0476$ W/cm°K [34]) is plotted (Fig. 10) for various diameters and thicknesses. The effects of a temperature dependent k (9) are readily observed in Fig. 10 where the curves deviate from a linear temperature rise with P [predicted using (8) with constant k]. The difference is substantial. For a 1-μm thick, 15-μm diameter absorber, and a constant $k_1 = k(T) = k(300°\text{C})$, (8) yields $\theta = 594\,°\text{C/W}$. The corresponding temperature would rise from 300 K to only 597 K at $P = 0.5$ W, where, from Fig. 10, the temperature would be closer to 1000 K when properly accounting for (9).

It should be emphasized that (8) implies that, given a PD with a fixed, RC-limited bandwidth, the minimum possible thermal impedance is determined only by the thermal conductivity of the absorber material. However, achieving this minimum will be determined by the effectiveness of achieving uniform illumination over the absorber area. This holds true for surface-illuminated as well as waveguide structures, although, in the case of traveling-wave design, the capacitance may not limit the bandwidth [17] since the effective area can exceed the area of a lumped-element RC-limited bandwidth PD. However, for PD's with traveling-wave design, other factors can quickly offset any improvement that larger effective areas

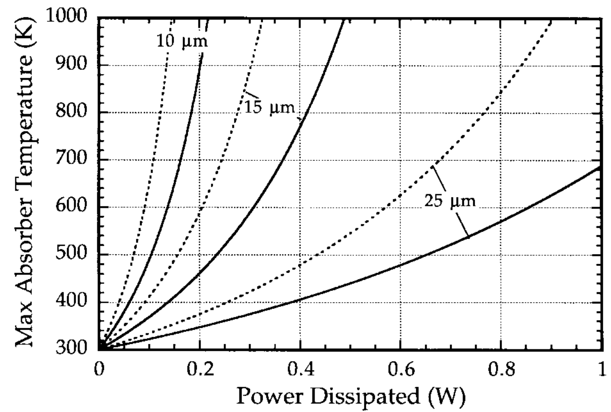

Fig. 10. Calculated maximum InGaAs absorber temperature versus power dissipated for absorber thicknesses of 1.0 μm (solid) and 1.5 μm (dashed) for heat source diameters of 10, 15, and 25 μm. The substrate side of the absorber is assumed to be at 300 K.

might help in reducing the absorber thermal impedance. The degrading factors of waveguide PD's will be addressed in Section VI.

While the absorber thermal impedance puts a lower limit on the total attainable thermal impedance, the material between the absorber and the final heat sink can contribute substantially to the total thermal impedance. For a circular heat source, radius h, mounted on a circular substrate, radius b, having a thickness d_2, (Fig. 3), the solution to Laplace's equation can be expressed in series form [37] as

$$\theta_{\text{sub}}(r, z) = \frac{d_2}{k_2 \pi b^2} + \frac{2}{k_2 \pi h b^2} \sum_{l=1}^{\infty} \cdot \frac{\sinh(\varphi_l (d_2 - z))}{\varphi_l^2 \cosh(\varphi_l d_2)} \frac{J_1(\varphi_l h) J_0(\varphi_l r)}{J_0^2(\varphi_l b)} \tag{12}$$

where the constants Φ_1 are determined by solutions of $J_1(\Phi_1 b) = 0$ and k_2 is the thermal conductivity of InP (k_2(300 K) $= 0.68$ W/cm K [33]). Equation (12) is plotted at r and $z = 0$ (the hottest point) in Fig. 11 for a 20 μm diameter heat source on the surface of a circular InP substrate (radius 500 μm) as a function of the substrate thickness. The summation in (12) was terminated when the contribution to the thermal impedance per additional term was reduced to below 1 part in 10^6 (approximately 10^4 to 10^5 terms). As is typical in power semiconductor devices [37], [38], the thermal impedance is a weak function of the substrate thickness when the thickness is larger than a few times the heat source diameter.

Comparing the results in Fig. 11 with (8)–(11), it is apparent that the substrate thermal impedance can be comparable to that of the absorber. Thus, both are important to the total thermal analysis. To include the thermal impedance of the InP substrate with the InGaAs absorbers from Fig. 10, a composite solution is formed. At each power level, the substrate thermal impedance is calculated with (12), thus yielding the temperature (at the heat source center) on the heat sink side of the absorber. This temperature is then used as the new heat sink temperature, T_o, (worst case) for the absorber in calculating

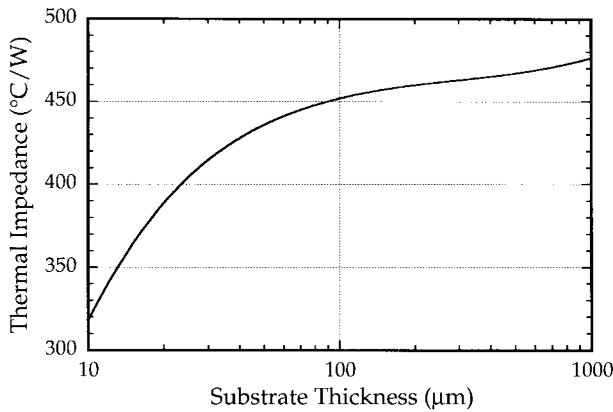

Fig. 11. Calculated thermal impedance versus substrate thickness from (12) for a 20-μm diameter heat source on a 1000-μm diameter InP substrate.

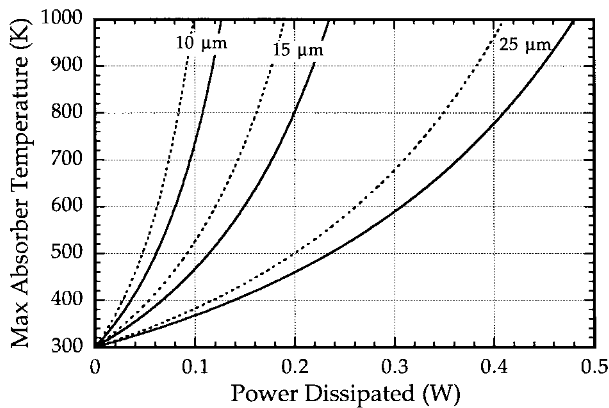

Fig. 12. Calculated maximum InGaAs absorber temperature versus power dissipated for absorber thicknesses of 1.0 μm (solid) and 1.5 μm (dashed) for heat source diameters of 10, 15, and 25 μm. The absorber is directly on top of a 1000-μm diameter, 200-μm thick InP substrate. The back side of the substrate is assumed to be at 300 K.

the maximum absorber temperature using (8)–(11). The results are plotted in Fig. 12 for the same size and thickness absorbers as in Fig. 10 where, for a 600–900 K maximum absorber temperature, the maximum permissible power that could be dissipated is reduced by approximately 50%. Thus, if a low thermal impedance from the InP substrate to the external heat sink [39] can be achieved, then the maximum power dissipated for a typical 20 GHz surface-illuminated p-i-n PD ($r = 12.5$ μm, $d_1 = 1$ μm) at failure would be approximately 0.2–0.4 W, in agreement with experimental results obtained in [8].

A closer examination of (12) reveals that the thermal impedance varies inversely with the absorber diameter. Thus, for PD's with a RC-limited bandwidth, there are thermal advantages to increasing the diameter. This is in contrast to the absorber thermal impedance which is independent of the RC-limited bandwidth PD dimensions. To quantify this, Fig. 13 plots the maximum power dissipated in a RC-limited (nominally 20 GHz) PD for a fixed maximum temperature rise of 300 and 600 °C. Note how the maximum possible power dissipation doubles when the physical diameter is increased from 10 μm (0.16 μm absorber thickness) to 25 μm (1.00 μm absorber thickness). At first glance, this would be an obvious trait to exploit, however, in the optimization for maximum compression current, the power dissipation must be weighed against the required voltage necessary to overcome space-charge effects. Recalling the results in Fig. 6, the compression current for p-side illuminated PD's is approximately the same for 0.16 and 1.0-μm long PD's. However, the results in Fig. 6 were calculated for a constant average electric field strength. The 0.16-μm long PD operates at only 16% the voltage of the 1.0-μm long PD, a 600% decrease in power dissipated for the same average current. Thus, any thermal impedance advantage that is gained by increasing the diameter (and hence thickness), is quickly lost because of the required voltage that is necessary to fully deplete the intrinsic-region and to overcome space-charge effects. This is also quantified in Fig. 13, where the maximum current of an RC-limited BW PD is calculated by dividing the power dissipated by the applied voltage necessary to yield an average electric field strength of 100 kV/cm (as in Fig. 6). This calculation is valid if the current is independent of intrinsic region thickness. This is true for p-side-illuminated PD's in the range of intrinsic region lengths from 0.2 to 1.25 μm (see Fig. 6). The dashed lines represent extrapolations of this calculation to longer absorbers for which the validity of this assumption is less valid. Therefore, to obtain maximum compression current, PD's should be fabricated with the thinnest absorber possible. This result has its limits since, as the absorber thickness decreases (recalling the results from Section II) the PD terminal voltage needs to be raised to allow for voltage transients across the load. Thus, when this added voltage is comparable to the voltage required to overcome space-charge effects, the extra voltage weighs more heavily on the total power dissipated. In addition, if the absorber is very thin, the added voltage could cause excessively high-electric fields, resulting in breakdown or avalanching effects. Nevertheless, the reduced absorption in thinner absorbing regions will dictate that double-pass or resonant cavity [40] absorber designs be used to obtain efficient high-current surface-illuminated PD's.

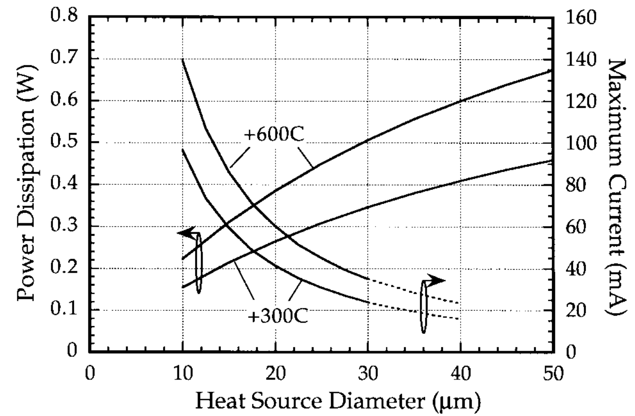

Fig. 13. Calculated power dissipation that results in α in peak absorber temperatures increase of 300 and 600° for a circular RC-limited 20 GHz bandwidth PD. An InGaAs absorber on an InP substrate (same substrate as used in Fig. 12) is assumed. Also plotted is the maximum photocurrent for a PD based on the calculated power dissipated and the applied voltage necessary to achieve an average electric field strength of 100 kV/cm.

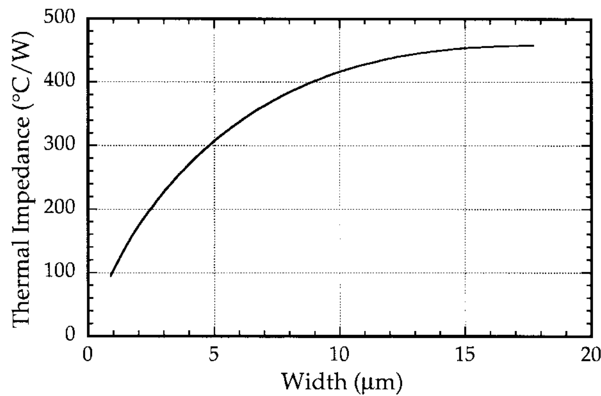

Fig. 14. Calculated thermal impedance of a rectangular heat source on a 200-μm thick, 886 × 886 μm square InP substrate versus heat source width. The rectangular heat source has a constant area of 314 μm^2.

VII. Comparisons Between Surface-Illuminated and Waveguide Photodiodes

Considerable effort has been focused in recent years toward the design of waveguide and traveling-wave PD's [14]–[17], [36]. At first glance it seems obvious that traveling-wave PD's should provide the highest current as the carrier and heat densities can be minimized since the bandwidth is not limited by capacitance, allowing larger surface areas to be exploited. However, waveguide structures may not be necessary, especially in low speed (<30 GHz) applications, since the full potential of surface-illuminated designs has yet to be realized. This is especially important when cost is considered owing to the potential difficultly of fiber coupling to the waveguide. This section will compare surface-illuminated to waveguide structures in terms of heat dissipation, space-charge effects, and the practical implementation of techniques to maximize compression current.

Ultimately, one advantage waveguide PD's have over surface-illuminated PD's is the decrease in thermal impedance due to the heat source being long and narrow. This can result in a reduced absorber-to-substrate thermal impedance as the absorber thermal impedance is fixed, given a RC-limited bandwidth as previously discussed. Although, if a traveling-wave design is employed with a response that is not limited by the lumped-element capacitance, lower absorber thermal impedances and lower space-charge effects could be achieved. Here the focus is with the thermal impedance improvements due to the heat source geometry and any improvements due to the traveling-wave design will just be an extension of the calculations performed here. Many methods have been used [37], [38], [41] to calculate the thermal impedance of rectangular heat sources common to semiconductor devices. Fig. 14 shows the thermal impedance for a rectangular heat source centered on a square InP die based on the formula in [37]. For a square heat source (17 × 17 μm), the thermal impedance is the same as the circular absorber (Fig. 11) as expected, since the thermal impedance is roughly a function of the heat source area. However, as the waveguide becomes long and thin, a reduction of 200–400% is achieved for waveguide widths below 3 μm.

The calculations in Fig. 14 assume a waveguide centered on the InP substrate. In practice, one facet of the waveguide is at the edge of the die to allow fiber coupling. Additional calculations show that, in this case where one end of the waveguide is within 10 μm of the edge, the thermal impedance increases slightly, about 10–20%, depending on the waveguide dimensions. Thus, in the limit of very narrow waveguides, the substrate thermal impedance is much smaller than the absorber thermal impedance and the limitations on the maximum power dissipation are determined primarily by the absorber (Fig. 10). Ideal RC-limited waveguide PD's could therefore potentially operate at twice the power dissipation of ideal surface-illuminated PD's, although this has not yet been experimentally observed [8].

Deviations from ideal operating conditions can quickly degrade the maximum power dissipation for both waveguide and surface-illuminated PD's. In the case of surface-illuminated PD's coupled with Gaussian-shaped beams, the current (hence heat source) is concentrated near the center of the absorber. For example, the results in Fig. 5 show that if the power is spread out such that the PD is operated at 98% of peak quantum efficiency ($r/r_o = 1.4$), the e^{-2} spot size, r_o, of the Gaussian beam is equal to the actual PD radius, r, divided by 1.4. Since most of the power in a Gaussian beam is concentrated within 70% of r_o, the majority of the heat is generated in only approximately 1/4 of the physical area. Thus, for a 25 μm diameter PD optimized at 98% quantum efficiency, the thermal impedance calculations for a 12.5 μm diameter PD should be used to calculate typical thermal impedances.

As for waveguide PD's, three important factors are responsible for limiting the available potential of these structures. The low total thermal impedance, resulting from long thin effective heat sources, can increase substantially if thick layers such as InGaAsP [15], [36], which has an even lower thermal conductivity [32] than InGaAs, are used to help dilute the light absorption and guide the light in the waveguide. These layers can be substantially thicker than the InGaAs absorber itself, and thus can completely eliminate the advantage of long, thin heat sources that waveguide PD's have over surface-illuminated PD's. The second limitation is the difficulty in designing the absorber to achieve uniform illumination [15] over the absorber area, since normally, the absorption distribution for a rectangular waveguide with constant absorption coefficient is a decaying exponential. This is important because any nonuniform carrier distribution will lead to localized heating and enhanced space-charge effects [17] nearest to the input of the waveguide. Last, the power density limitations of the input facet [16] need to be properly addressed to allow input power levels approaching 100 mW without facet damage.

VIII. Conclusions

In conclusion, we have outlined design considerations for gigahertz-bandwidth high-current p-i-n photodetectors utilizing InGaAs absorbers. Compression current measurements on two photodetectors were used to define two important parameters, the threshold voltage required for high-current operation and the slope of the compression current versus voltage

curve. Simulations of RC-limited-bandwidth photodetectors were then used to optimize designs which would minimize the threshold voltage and maximize the slope. These optimizations lead to higher compression currents at lower applied voltages and thus, less power dissipation, which is important since thermal damage can limit the maximum compression current. Lower threshold voltages were shown to be associated with p-side illumination, low intrinsic region doping densities, and thin absorber lengths. Higher slopes were shown to be associated with thinner absorbers and with lower photogenerated carrier densities (defocusing the light). A thermal model was also developed to quantify the thermal impedance of photodiodes. The model was used to show that spreading the generated heat out by increasing the absorber diameter was a weak effect compared to the space-charge advantages of thin absorbers, thus outweighing the thermal considerations for smaller, thinner absorbers. Finally, some comparisons were made between surface-illuminated and waveguide photodetectors to compare relative performance and to outline the steps required to obtain maximum performance from each structure.

ACKNOWLEDGMENT

The authors would like to thank D. Cooper and J. Dexter for their support.

REFERENCES

[1] C. Cox, III, E. Ackerman, R. Helkey, and G. E. Betts, "Techniques and performance of intensity-modulation direct-detection analog optical links," *IEEE Trans. Microwave Theory Tech.,* vol. 45, pp. 1375–1383, Aug. 1997.

[2] L. T. Nichols, K. J. Williams, and R. D. Esman, "Optimizing the ultrawideband photonic link," *IEEE Trans. Microwave Theory Tech.,* vol. 45, pp. 1384–1389, Aug. 1997.

[3] K. J. Williams, L. T. Nichols, and R. D. Esman, "Photodetector nonlinearity limitations on a high-dynamic range 3 GHz fiber optic link," *J. Lightwave Technol.,* vol. 16, pp. 192–199, Feb. 1998.

[4] K. J. Williams, M. L. Dennis, I. N. Duling, C. A. Villarruel, and R. D. Esman, "A simple high-speed high-output-voltage digital receiver," *IEEE Photon. Technol. Lett.,* vol. 10, pp. 588–590, Apr. 1998.

[5] Y. Miyamoto, M. Yoneyama, K. Hagimoto, T. Ishibashi, and N. Shimizu, "Ultra high speed optical receiver with uni-traveling-carrier photodiode acting as a logic IC driver," in *Conf. Lasers and Electron. Optics/Pacific Rim Tech. Dig.,* postdeadline paper PD2.10.

[6] K. J. Williams, R. D. Esman, and M. Dagenais, "Effects of high space-charge fields on the response of microwave photodetectors," *IEEE Photon. Technol. Lett.,* vol. 6, pp. 639–641, May 1994.

[7] G. A. Davis, R. E. Weiss, R. A. LaRue, K. J. Williams, and R. D. Esman, "A 920–1650 nm high-current photodetector," *IEEE Photon. Technol. Lett.,* vol. 8, pp. 1373–1375, 1996.

[8] J. Paslaski, P. C. Chen, J. S. Chen, C. M. Gee, and N. Bar-Chaim, "High-power microwave photodiode for improving performance of RF fiber optic links," in *Proc. SPIE, Photon. Radio Freq.,* Denver CO, 1996, vol. 2844, pp. 110–119.

[9] N. Shimizu, N. Watanabe, T. Furuta, and T. Ishibashi, "InP–InGaAs uni-traveling-carrier photodiode with improved 3 dB bandwidth of over 150 GHz," *IEEE Photon. Technol. Lett.,* vol. 10, pp. 412–414, Mar. 1998.

[10] J. Harari, G. Jin, J. P. Vilcot, and D. Decoster, "Theoretical study of p-i-n photodetectors power limitations from 2.5–60 GHz," *IEEE Trans. Microwave Theory Tech.,* vol. 45, pp. 1332–1336, Aug. 1997.

[11] K. J. Williams, R. D. Esman, R. B. Wilson, and J. D. Kulick, "Differences in p-side and n-side illuminated p-i-n photodiode nonlinearities," *IEEE Photon. Technol. Lett.,* vol. 10, pp. 132–135, Jan. 1998.

[12] D. Kuhl, F. Hieronymi, E. H. Bottcher, T. Wolf, D. Bimberg, J. Kuhl, and M. Klingenstein, "Influence of space charges on the impulse response of InGaAs metal-semiconductor-metal photodetectors," *J. Lightwave Technol.,* vol. 10, pp. 753–759, June 1992.

[13] K. J. Williams, R. D. Esman, S. Williamson, J. Valdmanis, K. Al-Hemyari, and J. V. Rudd, "Measurements of InGaAs metal-semiconductor-metal photodetector nonlinearities," *IEEE Photon. Technol. Lett.,* vol. 9, pp. 812–814, June 1997.

[14] A. R. Williams, A. L. Kellner, and P. K. L. Yu, "High frequency saturation measurements of an InGaAs/InP waveguide photodetector," *Electron. Lett.,* vol. 29, no. 14, pp. 1298–1299, 1993.

[15] S. Jasmin, N. Vodjdani, J.-C. Renaud, and A. Enard, "Diluted- and distributed-absorption microwave waveguide photodiodes for high efficiency and high power," *IEEE Trans. Microwave Theory Tech.,* vol. 45, pp. 1337–1341, Aug. 1997.

[16] V. M. Hietala, G. A. Vawter, T. M. Brennan, and B. E. Hammons, "Traveling-wave photodetectors for high-power, large-bandwidth applications," *IEEE Trans. Microwave Theory Tech.,* vol. 43, pp. 2291–2298, Sept. 1995.

[17] K. S. Giboney, M. J. W. Rodwell, and J. E. Bowers, "Traveling-wave photodetector design and measurements," *IEEE J. Select. Topics Quantum Electron.,* vol. 2, pp. 622–629, Sept. 1996.

[18] L. Y. Lin, M. C. Wu, T. Itoh, T. A. Vang, R. E. Muller, D. L. Sivco, and A. Y. Cho, "High-power high-speed photodetectors—Design, analysis, and experimental demonstration," *IEEE Trans. Microwave Theory and Tech.,* vol. 45, pp. 1320–1331, Aug. 1997.

[19] C. L. Goldsmith, G. A. Magel, B. M. Kanack, and R. J. Baca, "Principles and performance of traveling-wave photodetector arrays," *IEEE Trans. Microwave Theory Tech.,* vol. 45, pp. 1342–1350, Aug. 1997.

[20] K. J. Williams, R. D. Esman, and M. Dagenais, "Nonlinearities in p-i-n microwave photodetectors," *J. Lightwave Technol.,* vol. 14, pp. 84–96, 1996.

[21] R. R. Hayes and D. L. Persechini, "Nonlinearity of p-i-n photodetectors," *IEEE Photon. Technol. Lett.,* vol. 5, pp. 70–72, 1993.

[22] K. J. Williams and R. D. Esman, "Large-signal compression-current measurements in high-power microwave p-i-n photodiodes," *Electron. Lett.,* vol. 35, no. 1, pp. 82–84, 1999.

[23] P. L. Liu, K. J. Williams, M. Y. Frankel, and R. D. Esman, "Saturation characteristics of fast photodetectors," *IEEE Microwave Theory Tech.,* vol. 47, pp. 1297–1303, July 1999.

[24] K. J. Williams and R. D. Esman, "Photodiode DC and microwave nonlinearity at high currents due to carrier recombination nonlinearities," *IEEE Photon. Technol. Lett.,* vol. 10, pp. 1015–1017, July 1998.

[25] P. Hill, J. Schlafer, W. Powazinik, M. Urban, E. Eichen, and R. Olshansky, "Measurement of hole velocity in n-type InGaAs," *Appl. Phys. Lett.,* vol. 50, p. 1260, 1987.

[26] T. P. Pearsall, Ed., *GaInAsP Alloy Semiconductors.* New York: Wiley, 1982.

[27] T. H. Windhorn, L. W. Cook, and G. E. Stillman, "Temperature dependent electron velocity-field characteristics for $In_{0.53}Ga_{0.47}As$ at high electric fields," *J. Electron. Materials,* vol. 11, no. 6, pp. 1065–1082, 1982.

[28] T. H. Windhorn, L. W. Cook, T. J. Roth, and G. E. Stillman, "High field transport in GaAs, InP, and $In_xGa_{1-x}As_yP_{1-y}$," in *The Physics of Submicron Structures.* New York: Plenum, 1984, pp. 253–259.

[29] S. Adachi, *GaAs and Related Materials: Bulk Semiconducting and Superlattice Properties.* Singapore: World Scientific, 1994, p. 597.

[30] S. M. Sze, *Physics of Semiconductor Devices,* 2nd ed. New York: Wiley, 1981, p. 29.

[31] J. Paslaski, P. C. Chen, J. S. Chen, and N. Bar-Chaim, "High-power microwave photodiode for high-dynamic-range analog transmission," in *Proc. Optical Fiber Commun. Conf. Tech. Digest,* Optic. Soc. Amer., Washington, DC, 1994, paper ThG5, pp. 208–209.

[32] S. S. Kutateladze and V. M. Borishanskii, *A Concise Encyclopedia of Heat Transfer.* New York: Pergamon, 1966, pp. 11–44.

[33] S. Adachi, *Physical Properties of III–V Semiconductor Compounds InP, InAs, GaAs, GaP, InGaAs, and InGaAsP.* New York: Wiley, 1992, pp. 55–60.

[34] ——, "Thermal conductivity of InGaAs," in *Properties of Lattice-Matched and Strained Indium Gallium Arsenide,* P. Bhattacharya, Ed. New York: IEE Inspec, 1993, pp. 35–40.

[35] W. B. Joyce, "Thermal resistance of heat sinks with temperature-dependent conductivity," *Solid-State Electron.,* vol. 18, pp. 321–322, 1975.

[36] J. Harari, F. Journet, O. Rabii, G. Jin, J. P. Vilcot, and D. Decoster, "Modeling of waveguide PIN photodetectors under very high optical power," *IEEE Trans. Microwave Theory Tech.,* vol. 43, pp. 2304–2310, Sept. 1995.

[37] W. Liu, *Handbook of III–V Heterojunction Bipolar Transistors.* New York: Wiley, 1998, pp. 332–400.

[38] S. H. Wemple and H. Huang, "Thermal design of power GaAs FET's," in *GaAs FET Principles and Technology,* J. V. DiLorenzo, Ed. Norwood, MA: Artech House, 1982, pp. 313–347.

[39] H. F. Cooke, "Thermal effects and reliability, in *High-Power GaAs FET Amplifiers,* J. L. B. Walker, Ed. Norwood, MA: Artech House, 1993, pp. 227–261.
[40] K. Kishino, M. S. Unlu, J.-I. Chyi, J. Reed, L. Arsenault, and H. Morkoc, "Resonant cavity-enhanced (RCE) photodetectors," *IEEE J. Quantum Electron.,* vol. 27, pp. 2025–2034, Aug. 1991.
[41] R. D. Lindsted and R. J. Surty, "Steady-state junction temperatures of semiconductor chips," *IEEE Trans. Electron Devices,* vol. 19, pp. 41–44, Jan. 1972.

Keith J. Williams (S'86–M'97) was born in Lincoln, NE, on March 17, 1964. In 1987, he received the B.S. degree (cum laude) in electrical engineering from the University of Nebraska, Lincoln. He received the M.S. and Ph.D. degrees in electrical engineering from the University of Maryland, College Park, in 1989 and 1994, respectively. His doctoral dissertation research was conducted in the area of microwave p-i-n photodetector nonlinearities.

In 1987, he joined the Optical Techniques Branch of the Naval Research Laboratory (NRL), Washington, DC, where his research interests include characterization and performance of microwave-optical devices, microwave fiber-optic links and systems, high-speed optoelectronics, new concepts for solving microwave related problems with fiber-optic solutions, and high-current photodiodes.

Dr. Williams is a member of Tau Beta Pi.

Ronald D. Esman (S'82–M'85–SM'95) received the B.A. degree (magna cum laude) in physics and mathematics from Kalamazoo College, Kalamazoo, MI, in 1981. In 1980, he interned at Oak Ridge National Laboratory, Oak Ridge, TN, where his research included characterization and passivation of polycrystalline Si solar cells. He received the M.S. and D.Sc. degrees in electrical engineering from Washington University, St. Louis, MO, in 1983 and 1986, respectively. His doctoral thesis research was in the areas of fabrication, large-signal analysis, and characterization of high-speed electroabsorption avalanche photodetectors.

He joined Naval Research Laboratory (NRL), Washington, DC, in 1986, where he began work in the fields of high-speed optoelectronics, optical-microwave interactions, semiconductor laser noise and spectral characteristics, and fiber optics. He was with NIST, Boulder, CO, from 1990 to 1991, where he studied high-speed coherent optical transmission and measurement techniques at NTT Transmission Systems Laboratory, Yokosuka, Japan. From 1994 to 1998, he was Head of the Microwave Photonics Section at NRL, which is involved in RF array beam forming, photonics for radar, EW, and communications systems, remote sensing, photodetector nonlinearities, picosecond optical probing, and photonic analog-to-digital conversion. He is currently Head of the Photonics Technology Branch at NRL, which involves microwave photonics; >100 Gb/s sources, multiplexers and demultiplexers, and communication links; laser and amplifier development; and information technology. He has authored/coauthored 70 publications, has disclosed 20 inventions—ten patents granted and at least six others being filed.

Dr. Esman is a member of Sigma Xi, Phi Beta Kappa, and the Optical Society of America (OSA).